The Astrophysical Journal, 969:104 (24pp), 2024 July 10 https://doi.org/10.3847/1538-4357/ad4a72

Light-curve Structure and Hα Line Formation in the Tidal Disruption Event AT 2019azh

Sara Faris[1], Iair Arcavi[1], Lydia Makrygianni[1], Daichi Hiramatsu[2,3], Giacomo Terreran[4,5], Joseph Farah[4,5], D. Andrew Howell[4,5], Curtis McCully[4], Megan Newsome[4,5], Estefania Padilla Gonzalez[4,5], Craig Pellegrino[6], K. Azalee Bostroem[7,33], Wiam Abojanb[8], Marco C. Lam[9], Lina Tomasella[10], Thomas G. Brink[11], Alexei V. Filippenko[11], K. Decker French[12], Peter Clark[13], Or Graur[13,14], Giorgos Leloudas[15], Mariusz Gromadzki[16], Joseph P. Anderson[17,18], Matt Nicholl[19], Claudia P. Gutiérrez[20,21], Erkki Kankare[22], Cosimo Inserra[23], Lluís Galbany[20,21], Thomas Reynolds[22,24], Seppo Mattila[22,25], Teppo Heikkilä[22], Yanan Wang[26,27], Francesca Onori[28], Thomas Wevers[17,29], Eric R. Coughlin[30], Panos Charalampopoulos[31], and Joel Johansson[32]

[1] School of Physics and Astronomy, Tel Aviv University, Tel Aviv 69978, Israel; sarafaris452@gmail.com
[2] Center for Astrophysics, Harvard & Smithsonian, 60 Garden Street, Cambridge, MA 02138-1516, USA
[3] The NSF AI Institute for Artificial Intelligence and Fundamental Interactions, USA
[4] Las Cumbres Observatory, 6740 Cortona Drive, Suite 102, Goleta, CA 93117-5575, USA
[5] Department of Physics, University of California, Santa Barbara, CA 93106-9530, USA
[6] Department of Astronomy, University of Virginia, Charlottesville, VA 22904, USA
[7] Steward Observatory, University of Arizona, 933 North Cherry Avenue, Tucson, AZ 85721-0065, USA
[8] Atid Peki'in Comprehensive School, Peki'in, 2491400, Israel
[9] Institute for Astronomy, University of Edinburgh, Royal Observatory, Blackford Hill, Edinburgh, EH9 3HJ, UK
[10] INAF–Osservatorio Astronomico di Padova, Vicolo dell'Osservatorio 5, 35122 Padova, Italy
[11] Department of Astronomy, University of California, Berkeley, CA 94720-3411, USA
[12] Department of Astronomy, University of Illinois, 1002 W. Green Street, Urbana, IL 61801, USA
[13] Institute of Cosmology and Gravitation, University of Portsmouth, Portsmouth PO1 3FX, UK
[14] Department of Astrophysics, American Museum of Natural History, Central Park West and 79th Street, New York, NY 10024-5192, USA
[15] DTU Space, National Space Institute, Technical University of Denmark, Elektrovej 327, 2800 Kgs. Lyngby, Denmark
[16] Astronomical Observatory, University of Warsaw, Al. Ujazdowskie 4, 00-478 Warszawa, Poland
[17] European Southern Observatory, Alonso de Córdova 3107, Casilla 19, Santiago, Chile
[18] Millennium Institute of Astrophysics MAS, Nuncio Monsenor Sotero Sanz 100, Off. 104, Providencia, Santiago, Chile
[19] Astrophysics Research Centre, School of Mathematics and Physics, Queens University Belfast, Belfast BT7 1NN, UK
[20] Institut d'Estudis Espacials de Catalunya (IEEC), E-08034 Barcelona, Spain
[21] Institute of Space Sciences (ICE-CSIC), Campus UAB, Carrer de Can Magrans, s/n, E-08193 Barcelona, Spain
[22] Department of Physics and Astronomy, University of Turku, FI-20014 Turku, Finland
[23] Cardiff Hub for Astrophysics Research and Technology, School of Physics & Astronomy, Cardiff University, Queens Buildings, The Parade, Cardiff, CF24 3AA, UK
[24] Cosmic Dawn Center (DAWN), Niels Bohr Institute, University of Copenhagen, 2200, Denmark
[25] School of Sciences, European University Cyprus, Diogenes Street, Engomi, 1516 Nicosia, Cyprus
[26] National Astronomical Observatories, Chinese Academy of Sciences, 20A Datun Road, Beijing 100101, People's Republic of China
[27] Physics & Astronomy, University of Southampton, Southampton, Hampshire SO17 1BJ, UK
[28] INAF–Osservatorio Astronomico d'Abruzzo, via M. Maggini snc, I-64100 Teramo, Italy
[29] Space Telescope Science Institute, 3700 San Martin Drive, Baltimore, MD 21218, USA
[30] Department of Physics, Syracuse University, Syracuse, NY 13210, USA
[31] Department of Physics and Astronomy, University of Turku, Vesilinnantie 5, FI-20500, Finland
[32] Oskar Klein Centre, Department of Physics, Stockholm University, AlbaNova, SE-10691 Stockholm, Sweden
Received 2023 December 6; revised 2024 April 16; accepted 2024 April 17; published 2024 July 4

Abstract

AT 2019azh is a H+He tidal disruption event (TDE) with one of the most extensive ultraviolet and optical data sets available to date. We present our photometric and spectroscopic observations of this event starting several weeks before and out to approximately 2 yr after the *g*-band's peak brightness and combine them with public photometric data. This extensive data set robustly reveals a change in the light-curve slope and a possible bump in the rising light curve of a TDE for the first time, which may indicate more than one dominant emission mechanism contributing to the pre-peak light curve. Indeed, we find that the `MOSFiT`-derived parameters of AT 2019azh, which assume reprocessed accretion as the sole source of emission, are not entirely self-consistent. We further confirm the relation seen in previous TDEs whereby the redder emission peaks later than the bluer emission. The post-peak bolometric light curve of AT 2019azh is better described by an exponential decline than by the canonical $t^{-5/3}$ (and in fact any) power-law decline. We find a possible mid-infrared excess around the peak optical luminosity, but cannot determine its origin. In addition, we provide the earliest measurements of the Hα emission-

[33] LSSTC Catalyst Fellow.

line evolution and find no significant time delay between the peak of the *V*-band light curve and that of the Hα luminosity. These results can be used to constrain future models of TDE line formation and emission mechanisms in general. More pre-peak 1–2 days cadence observations of TDEs are required to determine whether the characteristics observed here are common among TDEs. More importantly, detailed emission models are needed to fully exploit such observations for understanding the emission physics of TDEs.

Unified Astronomy Thesaurus concepts: Accretion (14); Tidal disruption (1696); Supermassive black holes (1663); Ultraviolet transient sources (1854)

Supporting material: data behind figures, machine-readable table

1. Introduction

Supermassive black holes (SMBHs), with masses of $\gtrsim 10^6\,M_\odot$, are thought to reside in the center of most (if not all) large galaxies in the local Universe. While some SMBHs, known as active galactic nuclei (AGNs), accrete material that emits radiation, the majority are quiescent (e.g., Greene & Ho 2007; Mullaney et al. 2013) and thus difficult to study.

One of the few probes that can be used to study inactive SMBHs is the emission produced in a tidal disruption event (TDE). A TDE occurs when a star passes close enough to an SMBH for tidal forces to surpass the star's self-gravity, causing its disruption. In a full disruption, the star is torn apart and approximately half of it becomes gravitationally bound to the SMBH and eventually accretes onto it (Rees 1988; Evans & Kochanek 1989; Phinney 1989).

This transient phenomenon can not only serve to confirm the presence of an SMBH but also offers a promising tool for constraining its mass and perhaps even spin (e.g., Leloudas et al. 2016). As such, TDEs can potentially provide a more complete picture of the SMBH population. This can, in turn, help address some of the open questions regarding SMBHs, from accretion physics through their sub- and super-Eddington growth mechanisms to their scaling relations with global galaxy properties (such as the famous M–σ relation; e.g., Kormendy & Ho 2013). However, a main unresolved challenge lies in mapping TDE emission properties to SMBH characteristics.

The first discovered TDEs were searched for and detected in X-ray observations (e.g., Bade et al. 1996; Komossa & Greiner 1999; Cappelluti et al. 2009; Maksym et al. 2014; see Saxton et al. 2020 for a recent review), as the transient accretion disk was expected to emit at these wavelengths. However, in recent years, wide-field optical transient surveys have been discovering a growing number of TDEs in the optical bands, which are also bright in ultraviolet (UV) wavelengths (e.g., Gezari et al. 2006, 2012; van Velzen et al. 2011; Arcavi et al. 2014; see van Velzen et al. 2020 and Gezari 2021 for recent reviews). This surprising discovery has prompted work on theoretical models of TDEs to explain the optical/UV emission properties of these events.

Two main mechanisms for producing optical/UV emission in TDEs have been proposed. The first is the reprocessing of X-ray emission from an accretion disk by optically thick material surrounding the disk (e.g., Guillochon et al. 2014; Roth et al. 2016; Dai et al. 2018). The second model attributes the optical/UV emission to shocks formed between stellar debris streams as they collide around the apocenter before circularizing to form an accretion disk (Piran et al. 2015). Numerical simulations by Steinberg & Stone (2024) suggest a possible intermediate scenario whereby circularization can begin already at the pericenter, but the emission responsible for the light-curve peak is driven mainly by stream-disk shocks, which further circularizes the debris.

UV/optical TDEs are characterized by a luminous peak with a typical absolute magnitude of ~ -20 in the optical (a few events have been found down to peak magnitudes of ~ -17), rise timescales of days to weeks, and a smooth decline in the light curve lasting weeks to years (e.g., van Velzen et al. 2020, 2021). The blackbody temperature of these events remains high and approximately constant at $T \approx 10^4$ K (e.g., Gezari et al. 2012; Arcavi et al. 2014; van Velzen et al. 2020). Their bolometric luminosity sometimes follows a decline rate consistent with a $t^{-5/3}$ power law, which aligns with theoretical expectations for the mass return rate (Rees 1988; Evans & Kochanek 1989; Phinney 1989).

Spectroscopically, UV/optical TDEs show a strong blue continuum with broad ($\sim 10^4$ km s^{-1}) He II λ4686 (Gezari et al. 2012; Arcavi et al. 2014) and/or broad Balmer emission lines (e.g., Arcavi et al. 2014; Gezari et al. 2015; Hung et al. 2017), denoted H- He- or H+He-TDEs, accordingly (van Velzen et al. 2021). The width of the emission lines was initially attributed to Doppler broadening (Ulmer 1999; Bogdanović et al. 2004; Guillochon & Ramirez-Ruiz 2013). However, it was later suggested that at least some of the line broadening is caused by electron scattering (Roth & Kasen 2018). Some TDE spectra also exhibit He I λ5876 and/or heavier elements, such as [O III] λ5007 and N III $\lambda\lambda$4100, 4640 (sometimes blended with He II λ4686; Blagorodnova et al. 2017; Leloudas et al. 2019; Onori et al. 2019). Some of these lines have been attributed to the Bowen fluorescence mechanism (Bowen 1934), whereby extreme UV photons generate a specific cascade of lines. TDEs showing these lines are known as *Bowen TDEs*.

Some UV/optical TDEs are accompanied by X-ray and/or radio emission (e.g., Brown et al. 2017; Abolfathi et al. 2018; Saxton et al. 2020; Cendes et al. 2022; Liu et al. 2022; Bu et al. 2023). The X-rays are attributed to direct accretion emission, while the source of the radio emission is debated. It has been suggested to originate in outflows (Alexander et al. 2016), jets (van Velzen et al. 2016), and in the interaction between the unbound material and the interstellar medium (Krolik et al. 2016). In addition, delayed radio flares have recently been discovered to occur years after the optical peak in a few TDEs (Horesh et al. 2021). Their nature is also debated.

Here, we present and analyze extensive optical and UV observations, and available mid-infrared (MIR) observations, of the TDE AT 2019azh. X-ray, UV, and optical observations of this event were studied by Hinkle et al. (2021a), van Velzen et al. (2021), Liu et al. (2022), and Hammerstein et al. (2023), and long-duration radio emission by Goodwin et al. (2022) and Sfaradi et al. (2022). Spectropolarimetry of AT 2019azh was studied by Leloudas et al. (2022) and found to have the lowest polarization among the sample of TDEs studied.

We complement published optical and UV data of AT 2019azh with our own. The combined optical and UV data set presented here makes AT 2019azh one of the best-observed TDEs so far at these wavelengths, both photometrically and spectroscopically. We describe our observations in Section 2 and our analysis in Section 3, discuss our results in Section 4, and summarize in Section 5. We assume a flat ΛCDM cosmology, with $H_0 = 69.6\,\mathrm{km\,s^{-1}\,Mpc^{-1}}$, $\Omega_m = 0.286$, and $\Omega_\Lambda = 0.714$ (Wright 2006; Bennett et al. 2014).

2. Observations and Data Reduction

2.1. Discovery and Classification

AT 2019azh was discovered on 2019 February 22 at 00:28:48 (UTC dates are used throughout this paper) (MJD 58536.02; Stanek 2019) by the All-Sky Automated Survey for Supernovae (ASAS-SN; Shappee et al. 2014) as ASASSN-19dj with a *g*-band apparent magnitude of ∼16.2. The event was also detected by the Gaia photometric science alert team (Hodgkin et al. 2021)[34] as Gaia19bvo, and by the Zwicky Transient Facility (ZTF; Bellm et al. 2019) as ZTF17aaazdba and ZTF18achzddr.[35] The location of the event (Gaia J2000 coordinates $\alpha = 08^{\rm h}13^{\rm m}16\overset{\rm s}{.}96$, $\delta = +22°38'53\overset{''}{.}99$) is consistent with the center of the nearby galaxy KUG 0810+227, which has a redshift of $z = 0.0222240 \pm 0.0000071$ (Almeida et al. 2023), corresponding to a luminosity distance of 96.6 Mpc. This galaxy was preselected by French & Zabludoff (2018) as a possible TDE host, given its post-starburst properties (Arcavi et al. 2014).

The first few spectra of AT 2019azh showed a strong blue continuum without obvious features (Barbarino et al. 2019; Heikkila et al. 2019). The event was later classified as a TDE by van Velzen et al. (2019), based on its brightness, high blackbody temperature of ∼30,000 K, a position consistent with the center of the galaxy (with an angular offset between the ZTF coordinates of the event and the host nucleus of $0\overset{''}{.}07 \pm 0\overset{''}{.}31$), multiple spectra showing a strong blue continuum, and lack of spectroscopic features associated with a supernova (SN) or AGN.

2.2. Photometry

We obtained optical follow-up imaging of AT 2019azh with the Las Cumbres Observatory (Brown et al. 2013) global network of 1 m telescopes starting on MJD 58537.06 in the *BgVri* bands. Standard image processing was performed using the BANZAI automated pipeline (McCully et al. 2018). We combine our set of images with that of Hinkle et al. (2021a) and perform reference subtraction to remove host galaxy contamination using the High Order Transform of PSF and Template Subtraction algorithm (Alard & Lupton 1998; Alard 2000; Becker 2015) implemented by the `lcogtsnpipe` image subtraction pipeline (Valenti et al. 2016).[36] We use Las Cumbres Observatory images taken at MJD 59131.40 (∼596 days after discovery), after the transient faded, as references. Photometry was calibrated to the Sloan Digital Sky Survey (SDSS) Data Release 14 (Abolfathi et al. 2018) for the *gri* bands and to the AAVSO Photometric All-Sky Survey Data Release 9 (Henden et al. 2016) for the *BV* bands.

AT 2019azh was observed by all five ASAS-SN units in the *g* band, with the first detection recorded at MJD 58529.12. We use the ASAS-SN host-subtracted photometry as provided by Hinkle et al. (2021a).

The Swope (Bowen & Vaughan 1973) 1 m telescope at Las Campanas Observatory observed AT 2019azh in the *uBgVri* filters starting at MJD 58549.10. We use the Swope host-subtracted photometry as provided by Hinkle et al. (2021a).

We retrieved host-subtracted photometry from the Asteroid Terrestrial-impact Last Alert System (ATLAS; Tonry et al. 2018; Smith et al. 2020) in its *c* and *o* bands using the ATLAS public forced photometry server.[37] AT 2019azh was first detected by ATLAS on MJD 58529.37. More details regarding ATLAS data processing and photometry extraction can be found in Tonry et al. (2018) and Smith et al. (2020).

We retrieved ZTF host-subtracted photometry from the public ZTF forced photometry server.[38] The event was detected in the ZTF *g* and *r* bands starting from MJD 58512.26. A description of forced photometry processing for ZTF can be found in Masci et al. (2019).

The Neil Gehrels Swift Observatory (hereafter, Swift; Roming et al. 2005) observed AT 2019azh with all its UltraViolet and Optical Telescope (UVOT) filters (*b*, *v*, *u*, *uvw*1, *uvm*2, and *uvw*2), starting on MJD 58544.76 (PIs Arcavi, Hinkle, and Gezari). We take the host-subtracted extinction-corrected UVOT photometry from Hinkle et al. (2021b), which incorporates the new UVOT calibrations[39] not available in the earlier work by Hinkle et al. (2021a).

We retrieve the available MIR photometry obtained by the Wide-field Infrared Survey Explorer (WISE; Wright et al. 2010) NEOWISE Reactivation Releases (Mainzer et al. 2011, 2014) through the NASA/IPAC Infrared Science Archive. WISE obtains several images of each object during each observing phase (once every six months). We process these data using a custom Python script. The script filters out any individual observation identified as an upper limit and those with observational issues, such as being obtained close to the sky position of the Moon or suffering from poor frame quality. Weighted averages for each visit are then calculated per filter. We estimate the host galaxy flux and its uncertainty as the average and variance (respectively) of all pre-TDE observations and then subtract this flux from all observations.

We correct all optical and UV photometry for Milky Way extinction assuming a Cardelli et al. (1989) extinction law with $R_V = 3.1$ and Galactic extinction of $A_V = 0.122$ mag, as retrieved from the NASA Extragalactic Database[40] using the Schlafly & Finkbeiner (2011) extinction map. We correct the WISE MIR photometry for extinction using the Fitzpatrick (1999) extinction law with the corresponding coefficients from Yuan et al. (2013). All photometry is presented in the AB system (Oke 1974), except for the Las Cumbres *BV*-band data, which are presented in the Vega system.

The photometry obtained here from Las Cumbres, ATLAS, and ZTF are presented in Table 1. This photometry, together with the ASAS-SN and Swope photometry from Hinkle et al. (2021a), and the Swift photometry from Hinkle et al. (2021b),

[34] http://gsaweb.ast.cam.ac.uk/alerts

[35] The multiple names with prediscovery years are due to random image subtraction artifacts, which are common in galaxy nuclei, erroneously identified as possible transients.

[36] https://github.com/LCOGT/lcogtsnpipe

[37] https://fallingstar-data.com/forcedphot/

[38] https://ztfweb.ipac.caltech.edu/cgi-bin/requestForcedPhotometry.cgi

[39] https://www.swift.ac.uk/analysis/uvot/index.php

[40] https://ned.ipac.caltech.edu/extinction_calculator

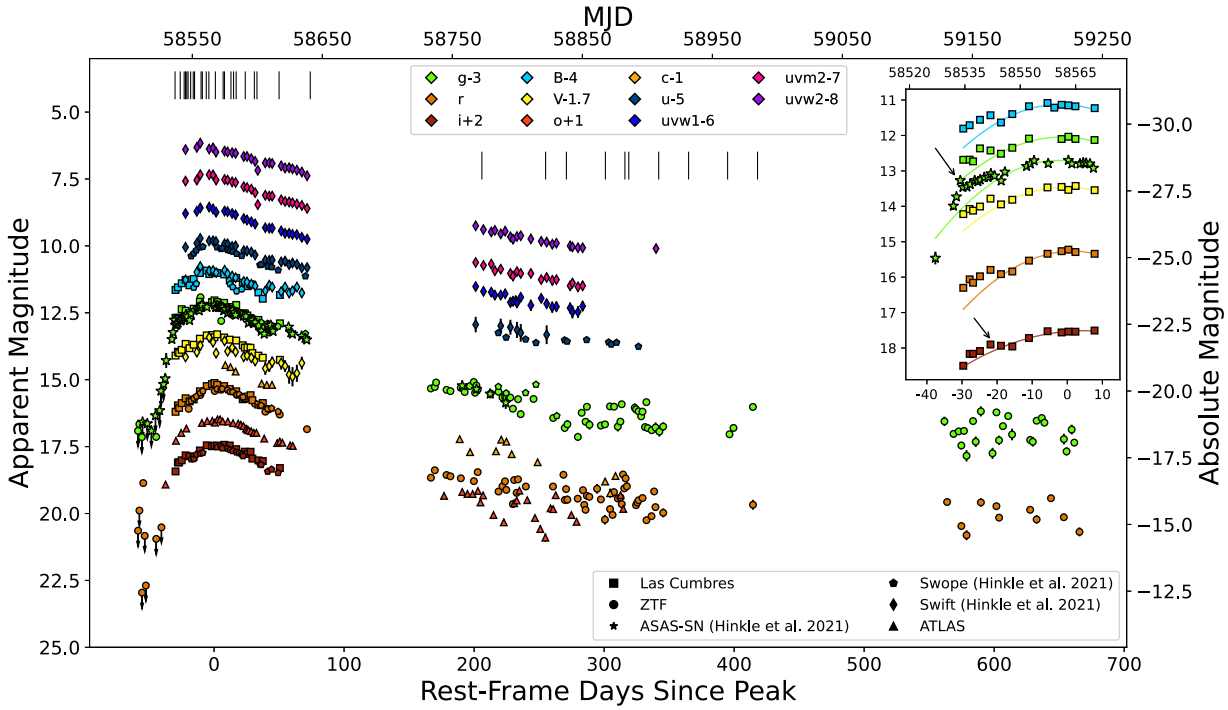

Figure 1. Milky Way extinction-corrected UV and optical light curves of AT 2019azh from Hinkle et al. (2021a, 2021b) and this work. Error bars denote 1σ uncertainties and are sometimes smaller than the marker size. Markers with arrows indicate 3σ nondetection upper limits. Black vertical lines indicate epochs with spectroscopic data. The inset displays the rise of the light curve in the data series, which covers the change in slope (at ~ -30 days from the peak) and possible bump (at ~ -20 days), marked with arrows (nondetections are omitted for clarity). The lines in the inset represent fits to the post-bump light curve, see the text for details.

Table 1
Host-subtracted and Milky Way Extinction-corrected Photometry and 3σ Nondetection Upper Limits

MJD	Phase (days)	Magnitude	Error	Filter	Source
58509.23	−55.93	>19.66	…	g	ZTF
58509.28	−55.88	>19.88	…	r	ZTF
58512.26	−52.90	18.86	0.05	*r*	ZTF
58522.18	−42.98	20.13	0.15	*g*	ZTF
58537.07	−28.09	16.19	0.02	*r*	Las Cumbres
58537.07	−28.09	15.69	0.09	*g*	Las Cumbres
58571.85	6.69	17.14	0.01	W1	WISE
58571.85	6.69	17.47	0.01	W2	WISE

(This table is available in its entirety in machine-readable form.)

is presented in Figure 1. The WISE photometry is also presented in Table 1 and in Figure A1 in Appendix A. We present all phases relative to *g*-band peak brightness at MJD 58566.70 ± 0.52 (as calculated in Section 3).

2.3. Spectroscopy

We obtained spectroscopic observations using the FLOYDS spectrographs (Sand et al. 2011) mounted on the Las Cumbres Observatory 2 m Faulkes Telescope South located at the Siding Spring Observatory in Australia and Faulkes Telescope North located at the Haleakalā Observatory in Hawaii, the ESO Faint Object Spectrograph and Camera (EFOSC2; Buzzoni et al. 1984) mounted on the 3.58 m ESO New Technology Telescope (NTT) as part of the extended Public ESO Spectroscopic Survey for Transient Objects (ePESSTO), the Asiago Faint Object Spectrographic Camera (AFOSC) mounted on the Copernico 1.82 m Telescope in Asiago, Mount Ekar, the Intermediate-dispersion Spectrograph and Imaging System (ISIS) mounted on the 4.2 m William Herschel Telescope (WHT), the Wide field reimaging CCD camera (WFCCD) mounted on the du Pont 2.5 m telescope at the Las Campanas Observatory, the Kast Double Spectrograph (Miller & Stone 1994) mounted on the Shane 3 m telescope at Lick Observatory, and the Alhambra Faint Object Spectrograph and Camera (ALFOSC) mounted on the 2.56 m Nordic Optical Telescope (NOT) through the second NOT Un-biased Transient Survey program.[41]

The FLOYDS spectra were processed and reduced using a custom `PYRAF`-based pipeline.[42] This pipeline, based on the `Image Reduction and Analysis Facility` (`IRAF`; Tody 1986, 1993) framework, removes cosmic rays and performs wavelength and flux calibration and rectification, flat-field correction, and spectrum extraction.

The Copernico 1.82 m Telescope spectra were reduced using a custom reduction pipeline based on IRAF tasks. After bias and flat-field correction, spectra were extracted and wavelength calibrated. Nightly sensitivity functions were derived from observations of spectrophotometric standard stars (also used to derive the corrections for the telluric absorption bands).

The NTT spectra were reduced using the Python-based `PESSTO` pipeline (Smartt et al. 2015).[43] This pipeline encompasses essential steps, including detector bias calibration, flat-field calibration, cosmic-ray removal, comparison lamp frames, and wavelength and flux calibrations. The first NTT

[41] https://nuts.sn.ie
[42] https://github.com/LCOGT/floyds_pipeline
[43] https://github.com/svalenti/pessto

spectrum, obtained on MJD 58539.16, is publicly available on the Transient Name Server[44] (Barbarino et al. 2019).

The WHT/ISIS spectrum was reduced using custom recipes executed in IRAF. The use of the medium-resolution gratings (R600B and R600R) results in a gap in wavelength coverage between the blue and red arms. Overscan correction, bias subtraction, flat-field correction, and cosmic-ray removal were performed. Wavelength calibration is derived from comparison lamp frames taken at the same position to correct instrument flexure. The optimal extraction algorithm of Horne (1986) is used to extract the one-dimensional spectra. A photometric standard star was observed on the same night to derive the flux calibration.

Observations with the WFCCD on the 2.5 m du Pont telescope were obtained using a 1.″65 (150 μm) slit and the blue grism. Average seeing conditions were ∼0.″5. Data were reduced and calibrated using custom Python routines and standard star observations.

The Lick/Kast spectra were taken with the 600/4310 grism, the 300/7500 grating, and the D57 dichroic. All observations were made with the 2.″0 slit. This instrument configuration has a combined wavelength range of ∼3600–10700 Å, and a spectral resolving power of $R \approx 800$. The data were reduced following standard techniques for CCD processing and spectrum extraction (Silverman et al. 2012) utilizing IRAF routines and custom Python and IDL codes.[45] Low-order polynomial fits to comparison lamp spectra were used to calibrate the wavelength scale, and small adjustments derived from night-sky lines in the target frames were applied. The spectra were flux calibrated and telluric corrected using observations of appropriate spectrophotometric standard stars observed on the same night, at similar airmasses, and with an identical instrument configuration.

The ALFOSC spectrum was reduced using the `foscgui`[46] pipeline. The pipeline performs overscan, bias, and flat-field corrections; spectrum extraction; wavelength calibration; flux calibration; and removal of telluric features with `IRAF` tasks as well as the removal of cosmic-ray artifacts using `lacosmic` (van Dokkum 2001).

All spectra were obtained with the slit oriented at or near the parallactic angle to minimize slit losses due to atmospheric dispersion (Filippenko 1982).

We retrieved the spectrum of the host galaxy from SDSS Data Release 18 (Almeida et al. 2023). The spectrum was obtained on 2003 October 30, and covers a wavelength range of 3700–9300 Å with a spectral resolution of $R \approx 2000$.

We calibrate all spectra of AT 2019azh (except for the WHT spectrum, owing to its wavelength gap) and that of the host galaxy to photometry and correct the TDE spectra for Milky Way extinction[47] using the `PySynphot` package (STScI Development Team 2013).[48]

A log of our spectroscopic observations is provided in Table 2; all spectra are presented in Figure 2 and will be made available through the Weizmann Interactive Supernova Data Repository (Yaron & Gal-Yam 2012).[49]

3. Analysis

3.1. Photometry

3.1.1. Light-curve Rise

The high-cadence pre-peak observations of AT 2019azh allow us to identify structure in its early optical light curve. First, we identify an abrupt change in the rising slope of the *g*-band light curve at ∼−30 days relative to the peak. We fit the rising *g*-band light curve with a linear function once between MJD 58520 and 58537, and once between MJD 58537 and 58560, finding a significant change in slope from 0.279 ± 0.014 mag day^{-1} in the first interval to 0.0323 ± 0.0042 mag day^{-1} in the second interval.

Second, a possible *bump* at ∼−20 days relative to the peak can be seen in the *BgVri* bands. While subtle, it is present in all bands that cover that epoch in the Las Cumbres and ASAS-SN data. We fit a second-order polynomial to the photometry after the bump, from −20 to 10 days relative to the peak, and plot it in the inset of Figure 1, extrapolating the fit to the bump epochs. The bump is clearly seen as an excess above this fit. Such structure was not previously robustly identified in a TDE, in part owing to the lack of high-cadence pre-peak observations for most events. However, indications for early light-curve structure were seen in at least two TDEs, which we discuss in Section 4.

3.1.2. Light-curve Peak

We fit a second-order polynomial to the host-subtracted Las Cumbres optical photometry and Swift UV photometry (except for the Swift *uvw*2 data, which does not cover enough of the rise to peak brightness) between MJD 58536 and 58596 to determine the peak time and magnitude in each band (the fits are displayed in Figure B1 in Appendix B). The best-sampled light curve around the peak is that in the *g* band for which we find a peak time of MJD 58566.70 ± 0.52 and a peak absolute magnitude of -19.82 ± 0.03. We use this peak time as a reference for all phase information in this paper. We also check the cross-correlation offset between the *g* light curve and the light curves in the bands mentioned above, in the same time range, using the `PyCCF` package[50] (Peterson et al. 1998).

Table 3 details the peak time and apparent magnitude from the fit to peak in each band. Figure 3 illustrates the peak times of each band in relation to their central wavelengths. The *uvm*2, *uvw*1, and *u*-band central wavelengths and filter widths are taken from Poole et al. (2008), while the central wavelengths and filter widths for the rest of the bands are from the Las Cumbres Observatory website.[51] We find consistent results between the peak time fit method and the cross-correlation method. Both show a monotonic peak time versus wavelength relation (also found in other TDEs; see Section 4), with the peak-fit method results having a Pearson correlation coefficient of 0.993, and a best-fit linear slope of $(2.16 \pm 0.10) \times 10^{-3}$ day Å^{-1}.

We find a significant MIR flare at 5.15 days after the *g*-band peak, with a W1 − W2 color of −0.32 mag, which is well

[44] http://www.wis-tns.org/

[45] https://github.com/ishivvers/TheKastShiv

[46] foscgui is a graphical user interface aimed at extracting SN spectroscopy and photometry obtained with FOSC-like instruments. It was developed by E. Cappellaro. A package description can be found at http://sngroup.oapd.inaf.it/foscgui.html.

[47] The host galaxy spectrum was already corrected for Milky Way extinction, assuming the Cardelli et al. (1989) extinction law and using the all-sky dust maps from Pan-STARRS (Green et al. 2018).

[48] https://pysynphot.readthedocs.io/en/latest/

[49] https://www.wiserep.org

[50] http://ascl.net/1805.032

[51] https://lco.global/observatory/instruments/filters/

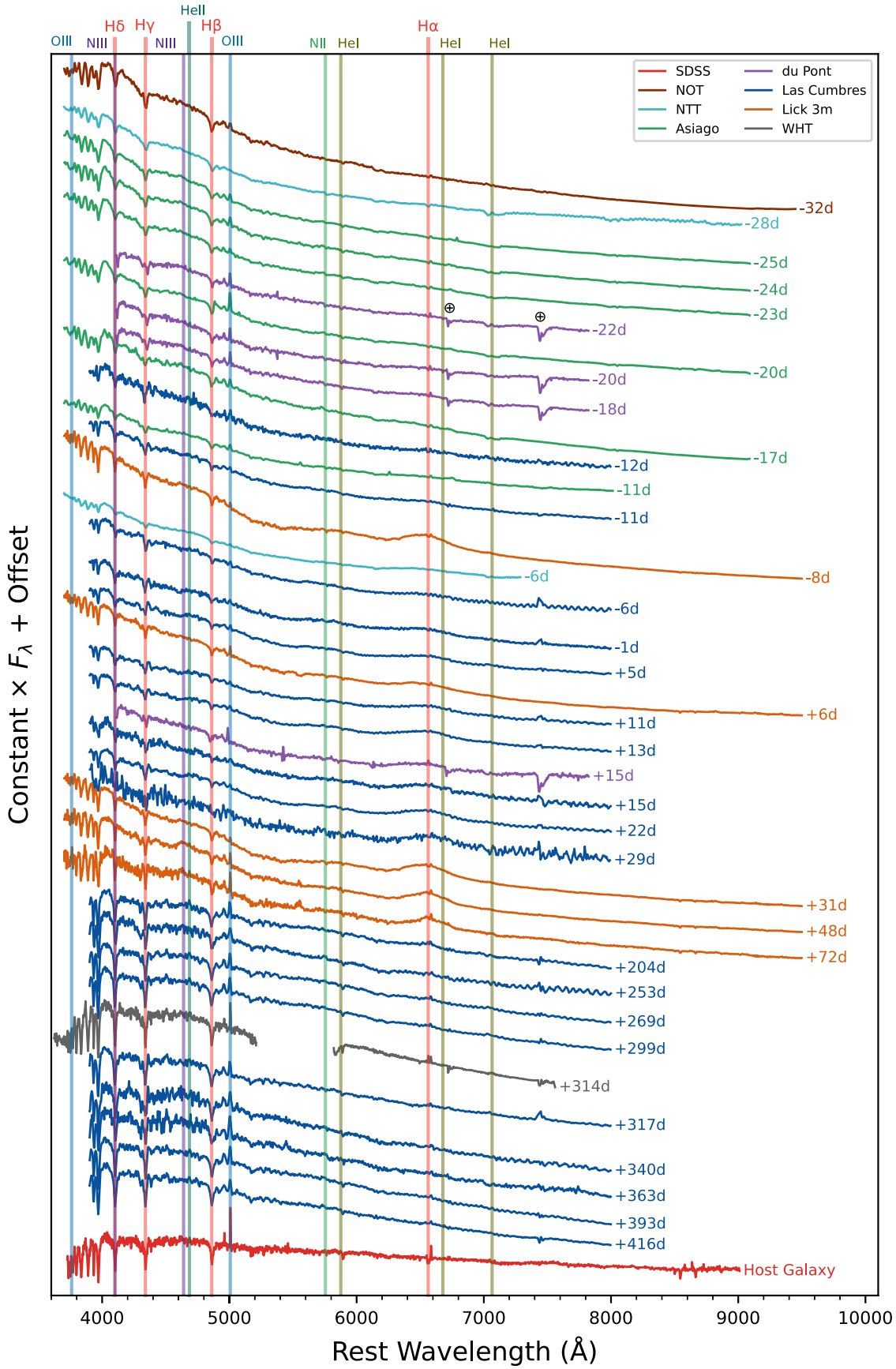

Figure 2. Spectroscopic evolution of AT 2019azh and the archival host galaxy spectrum from SDSS, after photometric calibration and Galactic extinction correction (except for the WHT spectrum). Notable TDE features, such as broad Hα and He II λ4686 emission lines, are evident in the spectra. We attribute the narrow Balmer absorption and narrow [O III] λ5007 emission lines, seen in all spectra, to the host galaxy. The phase of each spectrum in rest-frame days relative to the g-band light-curve peak is indicated and telluric lines are marked.

Table 2
Log of Spectroscopic Observations

Phase (days)	Telescope/Instrument	Slit Width (″)	Exposure Time (s)
−32	NOT/ALFOSC	1.3	900
−28	NTT/EFOSC2	1	300
−25	Copernico/AFOSC	1.69	1800
−24	Copernico/AFOSC	1.69	1500
−23	Copernico/AFOSC	1.69	1200
−22	du Pont/WFCCD	1.65	2700
−20	Copernico/AFOSC	1.69	2400
−20	du Pont/WFCCD	1.65	2700
−18	du Pont/WFCCD	1.65	2700
−17	Copernico/AFOSC	1.69	1800
−12	Las Cumbres/FLOYDS	2	1200
−11	Las Cumbres/FLOYDS	2	1200
−11	Copernico/AFOSC	1.69	2700
−8	Lick 3 m/Kast	2	2400
−6	NTT/EFOSC2	1	900
−6	Las Cumbres/FLOYDS	2	1200
−1	Las Cumbres/FLOYDS	2	1200
+5	Las Cumbres/FLOYDS	2	1200
+6	Lick 3 m/Kast	2	2400
+11	Las Cumbres/FLOYDS	2	1200
+13	Las Cumbres/FLOYDS	2	1200
+15	Las Cumbres/FLOYDS	2	1200
+15	du Pont/WFCCD	1.65	2700
+22	Las Cumbres/FLOYDS	2	1200
+29	Las Cumbres/FLOYDS	2	1200
+31	Lick 3 m/Kast	2	1500
+48	Lick 3 m/Kast	2	1800
+72	Lick 3 m/Kast	2	1800
+204	Las Cumbres/FLOYDS	2	3600
+253	Las Cumbres/FLOYDS	2	3600
+269	Las Cumbres/FLOYDS	2	3600
+299	Las Cumbres/FLOYDS	2	3600
+314	WHT/ISIS	1	2700
+317	Las Cumbres/FLOYDS	2	3600
+340	Las Cumbres/FLOYDS	2	3600
+363	Las Cumbres/FLOYDS	2	3600
+393	Las Cumbres/FLOYDS	2	3600
+416	Las Cumbres/FLOYDS	2	3600

Note. Phase is given in rest-frame days from the *g*-band peak brightness.

below the AGN threshold of $W1 - W2 = 0.8$ determined by Stern et al. (2012).

We calculate the expected MIR flux of a blackbody with the best-fit temperature and radius from day 8.09 after the *g*-band peak (the closest blackbody fit to the time of the WISE detections; see Section 3.1.3) using the `synphot` package (STScI Development Team 2018) with the WISE W1 and W2 filter bandpasses from Wright et al. (2010). We find that such a blackbody would produce a W1 and W2 AB magnitude of -16.32 ± 0.07 (the difference between the W1 and W2 magnitudes is negligible at the assumed temperature of $2.46 \pm 0.15 \times 10^4$ K derived in Section 3.1.3). The MIR detection extinction-corrected W1 and W2 AB magnitudes are -17.76 ± 0.13 and -17.45 ± 0.11, respectively, which are ∼1.1–1.5 mag brighter than the blackbody emission inferred from the optical and UV data. This excess may be due to a prompt dust echo, as observed, for example, by Newsome et al. (2024), but we cannot verify this without further data. We leave further analysis of the MIR emission from AT 2019azh to future work.

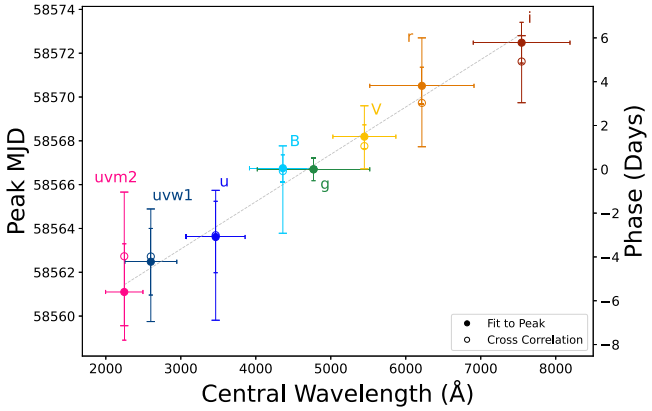

Figure 3. Light-curve peak MJD in various bands. Bluer bands peak earlier than redder bands. Filter widths are indicated with horizontal lines. The dashed gray line indicates a linear fit to the data.

3.1.3. Blackbody Fits

We fit the UV/optical photometry of AT 2019azh with a blackbody spectrum through the `SuperBol` fitting package[52] (Nicholl 2018), which uses the least-squares fitting method.[53] Here, we exclude ATLAS observations since the *c*- and *o*-band filters overlap with other filters, making them not fully independent observations. We restrict the fitting to epochs with available UV observations, as this helps reduce systematic errors when fitting blackbodies hotter than ∼30,000 K with optical data alone (Arcavi 2022), while linearly interpolating the optical light curves where necessary. We then calculate the bolometric luminosity using the Stefan–Boltzmann law, $L_{\rm bol} = 4\pi R^2 \sigma_{\rm SB} T^4$, with $\sigma_{\rm SB}$ the Stefan–Boltzmann constant, and R and T the blackbody radius and temperature from the fit, respectively.[54]

The evolution of the blackbody temperature, radius, and resulting bolometric luminosity are given in Table 4 and presented in Figure 4 in comparison to 15 other TDEs from van Velzen et al. (2021).[55] As with other TDEs, AT 2019azh exhibits constant high (∼25,000 K) temperatures with values at the high end, but consistent with the sample of van Velzen et al. (2021). Its blackbody radius evolution is also consistent with that of other TDEs and falls in the middle of the comparison sample. The bolometric luminosity of AT 2019azh is on the high end of the comparison sample, but still consistent with it. Our results are also roughly consistent with those of Hinkle et al. (2021b), but we obtain slightly lower temperatures and bolometric luminosities, especially at late times, compared to them.

We fit the post-peak bolometric light curve with a power law of the form $L \propto \left(\frac{t - t_0}{\tau}\right)^{-\alpha}$ and an exponential decline of the form $L \propto e^{-\frac{t-t_0}{\tau}}$. We perform the power-law fit in three

[52] https://superbol.readthedocs.io/en/latest/
[53] We convert the UVOT magnitudes to the Vega system, as required by SuperBol, using the conversions in https://swift.gsfc.nasa.gov/analysis/uvot_digest/zeropts.html.
[54] Here, we are not including any X-ray emission outside of the blackbody inferred from the optical and UV flux. Such emission is negligible around optical peak but comparable to what we measure at late times (Hinkle et al. 2021a).
[55] We compare to this sample since it is one of the largest samples of homogeneously analyzed TDE photometry to date.

Table 3
Peak MJD and Magnitude, Determined by Fitting a Second-order Polynomial to the Las Cumbres and Swift UV Photometry Around Peak Brightness

Band	Central Wavelength (Å)	Filter Width (Å)	Peak MJD	Phase (days)	Peak Magnitude	Cross-correlation Delay (days)
uvm2	2246	498	58561.10 ± 2.20	-4.70 ± 2.30	-20.49 ± 0.02	$-3.97^{+3.17}_{-2.93}$
uvw1	2600	693	58562.48 ± 1.52	-4.22 ± 1.66	-20.30 ± 0.02	$-3.98^{+2.97}_{-2.05}$
u	3465	785	58563.61 ± 1.63	-3.16 ± 1.77	-20.09 ± 0.02	$-3.01^{+3.88}_{-2.05}$
B	4361	890	58566.75 ± 0.61	0.05 ± 0.92	-19.91 ± 0.02	$-0.08^{+2.84}_{-1.15}$
g	4770	1500	58566.70 ± 0.52	0	-19.82 ± 0.03	0
V	5448	840	58568.19 ± 0.54	1.49 ± 0.87	-19.83 ± 0.02	$1.06^{+1.04}_{-1.84}$
r	6215	1390	58570.51 ± 0.85	3.81 ± 1.09	-19.68 ± 0.03	$3.03^{+2.00}_{-2.97}$
i	7545	1290	58572.48 ± 0.93	5.78 ± 1.15	-19.47 ± 0.02	$4.92^{+1.88}_{-1.18}$

Note. Phases are given relative to the *g*-band peak, and cross-correlation delays are given relative to the *g* light curve.

Table 4
Blackbody Temperature and Radius, and Resulting Bolometric Luminosity

Phase	T_{BB} (10^4 K)	R_{BB} (10^{14} cm)	L_{bol} (10^{44} erg s^{-1})
–21.94	2.55 ± 0.13	7.45 ± 0.43	1.66 ± 0.40
–13.25	2.75 ± 0.15	7.05 ± 0.45	2.03 ± 0.52
–10.59	2.83 ± 0.16	7.33 ± 0.45	2.46 ± 0.62
–3.75	2.49 ± 0.10	8.08 ± 0.38	1.80 ± 0.33
–0.76	2.55 ± 0.12	7.91 ± 0.43	1.88 ± 0.40
1.37	2.54 ± 0.17	7.70 ± 0.63	1.77 ± 0.56
1.58	2.36 ± 0.16	7.98 ± 0.68	1.42 ± 0.45
8.09	2.46 ± 0.15	7.87 ± 0.56	1.61 ± 0.45
10.40	2.43 ± 0.15	7.93 ± 0.59	1.55 ± 0.44
13.92	2.51 ± 0.18	7.38 ± 0.63	1.55 ± 0.51
16.57	2.50 ± 0.17	7.36 ± 0.61	1.51 ± 0.49
22.83	2.56 ± 0.18	6.71 ± 0.56	1.38 ± 0.45
25.35	2.62 ± 0.19	6.46 ± 0.55	1.40 ± 0.47
28.66	2.68 ± 0.22	6.06 ± 0.57	1.34 ± 0.50
31.59	2.63 ± 0.21	5.93 ± 0.55	1.19 ± 0.44
33.64	2.10 ± 0.17	7.00 ± 0.70	0.68 ± 0.26
39.42	2.94 ± 0.28	4.93 ± 0.51	1.29 ± 0.56
42.47	2.97 ± 0.32	4.85 ± 0.56	1.30 ± 0.64
44.72	2.54 ± 0.19	5.91 ± 0.47	1.03 ± 0.35
51.63	2.85 ± 0.25	4.86 ± 0.47	1.10 ± 0.45
54.62	2.81 ± 0.25	4.79 ± 0.47	1.02 ± 0.41
57.74	2.98 ± 0.25	4.45 ± 0.40	1.10 ± 0.42
60.33	3.00 ± 0.28	4.34 ± 0.44	1.08 ± 0.45
63.72	3.02 ± 0.29	4.21 ± 0.44	1.05 ± 0.46
67.50	3.05 ± 0.26	4.03 ± 0.38	1.00 ± 0.39
71.57	2.84 ± 0.23	4.19 ± 0.38	0.81 ± 0.30
201.24	3.13 ± 0.40	1.49 ± 0.19	0.15 ± 0.09
220.51	2.88 ± 0.29	1.44 ± 0.15	0.10 ± 0.05
223.89	2.73 ± 0.28	1.52 ± 0.16	0.09 ± 0.04
227.94	2.32 ± 0.16	1.76 ± 0.14	0.06 ± 0.02
232.99	2.60 ± 0.33	1.52 ± 0.21	0.08 ± 0.04
260.19	2.68 ± 0.56	1.25 ± 0.26	0.06 ± 0.05
275.68	2.62 ± 0.39	1.26 ± 0.19	0.05 ± 0.04
283.51	2.63 ± 0.38	1.23 ± 0.19	0.05 ± 0.03

Note. Phases are given relative to *g*-band peak brightness.

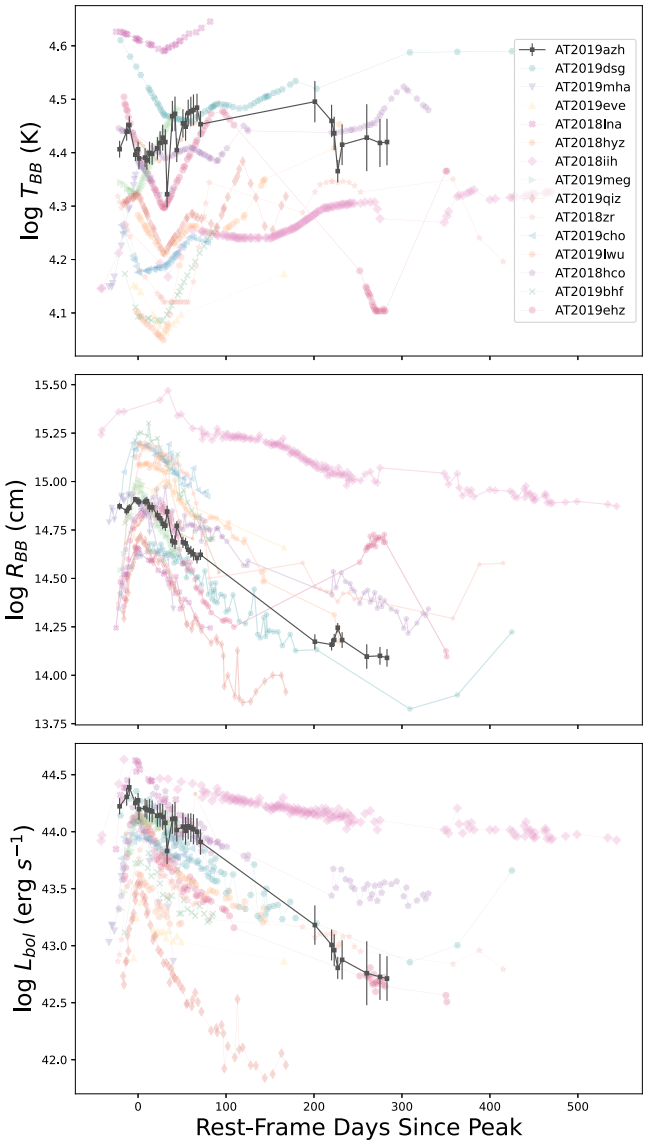

Figure 4. Blackbody temperature (top), radius (middle), and inferred bolometric luminosity (bottom) evolution obtained using `SuperBol` for AT 2019azh (black), compared to a sample of TDEs from van Velzen et al. (2021). The temperature, radius, and bolometric luminosity of AT 2019azh are consistent with those of other UV/optical TDEs. The van Velzen et al. (2021) measurements assume a parametric time evolution and hence are smoother.

(The data used to create this figure are available.)

different ways: once with the power-law index fixed to the canonical $\alpha = 5/3$ value and free t_0, once with free α and fixed t_0 (set to the best-fit value of -60 days from the peak, found by MOSFiT below), and once with free α and free t_0. The latter fit requires an unphysical t_0 of order 10^5 days before the peak to match the data, and the other two power-law fits (yielding

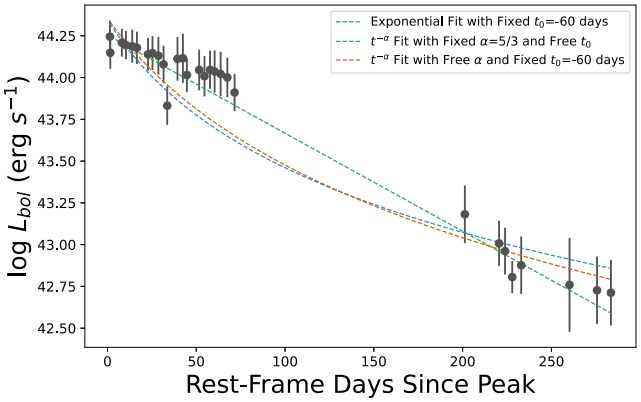

Figure 5. Power-law and exponential fits to the bolometric luminosity decline. The data are better represented by an exponential decline rather than a power law.

$\alpha = 2.06 \pm 0.11$ and $t_0 = -41.49 \pm 5.87$ days) are unable to match the data at all. The exponential decline, on the other hand, does match the data well. The different fits are shown in Figure 5. We conclude that the bolometric light-curve decline of AT 2019azh is better described by an exponential than a power law, similar to what was seen for ASASSN-15oi (Holoien et al. 2016a) and iPTF16fnl (Blagorodnova et al. 2017). Specifically, it does not fit the canonical $t^{-5/3}$ decline quoted for some TDEs.

3.1.4. TDE Model Fits

As mentioned in Section 1, there are currently two main models for the source of UV/optical emission in TDEs: reprocessing of X-rays from a rapidly formed accretion disk, and shock emission from debris stream collisions during the circularization process. We fit our photometry to the X-ray reprocessing model with the Modular Open Source Fitter for Transients (MOSFiT; Guillochon et al. 2018), and to the stream collision model with the TDEMass package (Ryu et al. 2020).

The MOSFiT TDE model (Mockler et al. 2019) is based on hydrodynamical simulations for converting the mass-fallback rate from the disrupted star to a bolometric flux. This conversion is related to the accretion rate through the viscous timescale $T_{\rm viscous}$, and it assumes a constant efficiency parameter ϵ. The reprocessing layer is assumed to be a simple blackbody photosphere with radius $R_{\rm phot}$.

The free parameters of the model are the BH mass ($M_{\rm BH}$); the mass of the disrupted star ($M_\star$); the viscous timescale ($T_{\rm viscous}$); the efficiency (ϵ); the blackbody photospheric radius $R_{\rm phot} \propto R_{\rm ph,0} \times L^{\,l}$ (where $R_{\rm ph,0}$ and l are free parameters and L is the bolometric luminosity); the scaled impact parameter (b), which is a proxy for the physical impact parameter $\beta \equiv R_{\rm t}/R_{\rm p}$ (with $R_{\rm t}$ the tidal radius and $R_{\rm p}$ the orbit pericenter); the time of first fallback ($t_{\rm exp}$); the host galaxy column density ($n_{\rm H}$); and a white-noise parameter (σ). We use the default priors from MOSFiT, as given by Mockler et al. (2019).

We utilize the nested sampling method,[56] implemented by DYNESTY (Speagle 2020), for the fit. As with the blackbody fits, here we also exclude the ATLAS bands. We further exclude observations more than 1 yr after discovery because the assumption of a blackbody photosphere made by MOSFiT might not be valid at such late times if the reprocessing material starts to become optically thin. We use the default MOSFiT termination criterion of a potential scale reduction factor of 1.1.

No formal goodness of fit metric is produced by this fitting procedure. The model matches the observations reasonably well in some regions and deviates from the data in others, as can be seen in Figure 6. Table 5 presents the best-fit parameters obtained from the fit; the posterior distributions, which are well converged, are displayed in Figure C1 in Appendix C. The efficiency parameter approaches its maximum allowed value, which affects the stellar mass parameter owing to their degeneracy (Mockler & Ramirez-Ruiz 2021). The impact parameter is $b = 0.99^{+0.01}_{-0.03}$, suggesting that the star is almost fully disrupted.

As Mockler et al. (2019) pointed out, this model includes several simplifications of the complex physics involved. For instance, assuming solar-composition polytropes instead of more realistic stellar density profiles that take into account the stellar metallicity, age, and evolutionary stage, could introduce systematic uncertainties in determining the stellar mass. Mockler et al. (2019) quantified these and other systematic uncertainties arising from some of the model simplifications, and we include these uncertainties in the total error estimates in Table 5.

In TDEMass (Ryu et al. 2020),[57] the mass of the disrupted star and the disrupting SMBH are estimated by numerically solving two nonlinear equations (Equations (11) and (12) of Ryu et al. 2020) and interpolating within precalculated tables of the peak bolometric luminosity ($L_{\rm obs}$) and the temperature at this peak ($T_{\rm obs}$). The equations include two parameters that determine the size and energy dissipation area of the emitting region: c_1, related to the apocenter distance for the orbit of the most tightly bound debris, and $\Delta\Omega$, the solid angle of the area where shocks dissipate a significant amount of energy. The values of these parameters are not well constrained, and the default model values of $c_1 = 1$ and $\Delta\Omega = 2\pi$ are assumed.

From our SuperBol fit, we find a peak luminosity of $L_{\rm obs} = 2.46 \pm 0.62 \times 10^{44}$ erg s^{-1} and a temperature at this peak of $T_{\rm obs} = 28{,}300 \pm 1550$ K. With these values, we obtain from TDEMass a BH mass of $M_{\rm BH} = 2.5^{+0.29}_{-0.24} \times 10^6\ M_\odot$ and a stellar mass of $M_\star = 4.8^{+4}_{-2.5}\ M_\odot$. Figure D1 in Appendix D displays the degeneracy between these two parameters. We

Table 5
Best-fit Parameters Obtained from the MOSFiT Fit with 1σ Confidence Intervals

Parameter	Best-fit Value	Total Error	Units
$\log(M_{\rm BH})$	$7.21^{+0.02}_{-0.02}$	± 0.20	$M_\odot$
$M_\star$	$0.1000^{+0.0002}_{-0.0002}$	± 0.66	$M_\odot$
$\log(T_{\rm viscous})$	$0.44^{+0.14}_{-0.42}$	± 0.43	day
$\log(\epsilon)$	$-0.47^{+0.05}_{-0.08}$	± 0.68	⋯
$\log(R_{\rm ph,0})$	$0.38^{+0.07}_{-0.05}$	± 0.4	⋯
l	$1.72^{+0.05}_{-0.06}$	± 0.2	⋯
b	$0.99^{+0.01}_{-0.03}$	± 0.35	⋯
$t_{\rm exp}$	$-6.95^{+1.24}_{-1.00}$	± 15	day
$\log(n_{\rm H})$	$20.66^{+0.03}_{-0.04}$	⋯	cm^{-2}
$\log(\sigma)$	$-0.45^{+0.01}_{-0.01}$	⋯	⋯

Note. The "Total Error" column includes systematic errors estimated by Mockler et al. (2019) due to some of the simplifying assumptions in the model.

[56] This method is typically employed for models with 10 or more parameters, as is the case here.

[57] https://github.com/taehoryu/TDEmass